RSC Advances

ROYAL SOCIETY OF CHEMISTRY

www.rsc.org/advances

Journal Name

ARTICLE

Fabrication and Photoactivity of Short Rod-shaped Mesoporous SiO_2@TiO_2 Composites with TiO_2 Shell

Received 00th January 20xx,
Accepted 00th January 20xx

DOI: 10.1039/x0xx00000x

www.rsc.org/

Pei Cao, Guowei Zhou,* Yixian Ren, and Hong Xiao

This paper presents an improved strategy for synthesizing short rod-shaped mesoporous SiO_2@TiO_2 composites containing TiO_2 shell by using short rod-shaped mesoporous SiO_2-polyglycidyl methacrylate (PGMA)-polyoligo(ethylene glycol) methyl ether methacrylate (PEGMA) as template and tetrabutyl titanate (TBT) as titanium source. SiO_2-PGMA-b-PEGMA rods were initially fabricated through grafting GMA and EGMA onto the surface of the halogen functional group of mesoporous SiO_2 using activators regenerated by electron transfer atom transfer radical polymerization. TBT was hydrolyzed with the PEGMA chain through hydrogen bonding. The rod-shaped mesoporous SiO_2@TiO_2 structure was finally acquired through calcination. Characterization results indicated that the amphiphilic block copolymer was grafted onto the mesoporous SiO_2 surface. Moreover, the TiO_2 samples existed only in the anatase phase, and the prepared SiO_2@TiO_2 exhibited bimodal nanoporous structures. The synthesized short rod-shaped mesoporous SiO_2@TiO_2 materials demonstrated higher specific surface area and absorption rate than samples prepared from non-mesoporous or unmodified rod-shaped SiO_2. These characteristics effectively enhanced the photocatalytic activity of the composite. The photocatalytic activity of the fabricated composite was then tested on rhodamine B photodegradation.

Introduction

Since the discovery of mesoporous SiO_2 in the early 1990s,[1] mesoporous materials have gained global interest because of their potential, wide range, technologically advanced and conventional applications.[2] Mesoporous materials features high specific area, uniform and tunable pore size (2–50 nm), and high pore volume and are thus suitable for heterogeneous catalysis, separation processes, biomedical systems, and host-guest chemistry.[3–5] In particular, mesoporous SiO_2 prepared from block copolymer-template has been widely used because of its larger pores and thicker walls than other organic-templated materials. A typical example of copolymer-templated mesoporous SiO_2 materials is SBA-15, which possesses a highly ordered hexagonal mesostructure, large pores, and remarkable hydrothermal stability.[6, 7] Therefore, SBA-15 exhibits potential in diverse applications, such as catalysis, sorption, and advanced material design.[8, 9]

Functionalization of mesostructured SiO_2, such as MCM-41 and SBA-15, has attracted considerable research interest.[10] A commonly investigated functionalized organic-inorganic hybrid material is polymer/SiO_2 nanocomposites, which exhibit combined advantages resulting from the polymer and mesoporous SiO_2. Hence, covering a SiO_2 surface with different polymers is a potential strategy for incorporating various organic functional groups to modify material properties and facilitate novel applications.[11, 12] Through integration of different organic moieties or polymers on the exterior or interior surface of mesoporous materials, penetration of selective molecules with specific sizes and chemical properties into mesopores can be precisely controlled. Nevertheless, functionalization of mesoporous SiO_2 through polymer covering presents two difficulties:[13] achievement of polymers covalently linked to inorganic materials and prevention of destroying the SiO_2 pore system by infilling with excess polymer. As such, activators regenerated through electron transfer-atom transfer radical polymerization (ARGET ATRP) based on reversible termination can be used to maintain the mesoporosity of SiO_2; this technique allows control of molecular weight, molecular weight distribution, and structure of the polymer obtained.[14] ARGET ATRP is a “green” procedure that uses a low concentration of catalyst present in the system.[15] A new ATRP initiating system was developed to facilitate solution and emulsion ATRP in aqueous media. The proposed system used excessive reducing agents, such as ascorbic acid, to ensure rapid reduction of Cu(II) to Cu(I) in the polymerization system, followed by catalytic polymerization of the ATRP monomer.[16] Cheesman et al.[17] produced pH-responsive brush-modified particles by growing poly(2-(diethylamino)ethyl methacrylate) [poly(DEA)] brushes on 120 nm SiO_2 particles through surface-initiated ARGET ATRP; in this study, which is the first to apply surface-initiated ARGET ATRP to grow poly(DEA) brushes, proof-of-concept hybrid particles

Key Laboratory of Fine Chemicals in Universities of Shandong, School of Chemistry and Pharmaceutical Engineering, Qilu University of Technology, Jinan 250353, Shandong, People’s Republic of China. E-mail: gwzhou@qlu.edu.cn, guoweizhou@hotmail.com

Electronic Supplementary Information (ESI) available: [FT-IR spectra Figures, TGA Figures, HRTEM Figures, FESEM Figures, and EDS Figures of different samples]. See DOI: 10.1039/x0xx00000x

for deployment were used as in situ rheology-modifying agents. Kruk et al.[18] described the grafting of PMMA through ARGET ATRP on SBA-15 SiO_2 with large mesopores (14 and 22 nm); the results showed that the dispersity of the grafted chains increased up to 2.1 with increasing polymer molar mass, and the grafting density and initiator efficiency of the synthesized material were 2 to 3 times lower than those of polyacrylonitrile grafted through normal ATRP. Cao et al.[19] demonstrated that ARGET ATRP is a convenient strategy for grafting functional polymers from a concave surface of ordered mesoporous SiO_2. In this study, SBA-15 silica containing cylindrical mesopores with a diameter of 24 nm was used as support, and poly(N-isopropylacrylamide) and poly[2-(dimethylamino)ethyl methacrylate], which exhibit stimulus-responsive properties, were used as grafted polymers. The results, along with the findings from previous reports of the same team,[20, 21] demonstrated that ARGET ATRP is a simple but effective approach for fabricating well-defined SiO_2/polymer nanocomposites.

TiO_2 nanomaterials, which features excellent electrical, optical, and photocatalytic properties, have been extensively applied in dye-sensitized solar cells,[22–24] water splitting,[25] optoelectronic devices,[26, 27] and photodegradation of organics.[28] TiO_2 materials have also been used as a photocatalyst for hazardous organic substance removal because of their chemical/photocorrosion stability, low cost, nontoxicity, and diverse preparation methods.[29, 30] Effective adsorption of reactants in well-designed porous materials plays an important role during catalysis. Nevertheless, the relatively low adsorption ability of TiO_2 results in poor photocatalytic activity.[31] Therefore, the adsorption capacity of catalysts must be enhanced to efficiently improve photocatalytic activity. Several materials, such as zeolite, mesoporous SiO_2 polymer matrix, and carbon materials,[32–35] have been explored as TiO_2 supports. A catalyst must be designed using the rational combination of the adsorption and photocatalytic sites at the nanoscale level to elucidate adsorption-assisted photocatalysis. The use of SiO_2 particles as scaffold for TiO_2 particles have been reported in various studies. Zhao et al.[36] successfully prepared a tunable-void SiO_2–TiO_2 core–shell structure using a modified SiO_2 solid sphere as template. Li et al.[37] reported the use of sulfuric acid as a catalyst for the facile and homogeneous synthesis of core–shell SiO_2@TiO_2 nanocomposites. Li et al.[38] prepared a series of raspberry-like SiO_2–TiO_2 nanoparticles by the one-pot sol–gel method. Compared with the SiO_2 particles, the mesoporous silica with incorporated titania was beneficial because of its high specific surface, tunable pore size, and high pore volume. Hence, the mesoporous SiO_2 support modified by the TiO_2 nanoparticles introduced more catalytic sites and contact areas. As such, the support largely enhanced the photocatalytic activity of the TiO_2 nanocrystals.[32,34] Furthermore, the mesoporous SiO_2 materials possessed good thermal and hydrothermal stability. SBA-15 functions as a good host for photocatalytic reactions because this mesoporous SiO_2 sieve possesses uniform hexagonal pores and high surface area.[39, 40] Overall, fabrication of well-defined mesoporous structured materials, such as TiO_2-modified SBA-15, is a promising method for achieving high photocatalytic activity because the ordered mesopore channels facilitate fast intraparticle molecular transfer.

Direct and post-synthesis techniques are used to prepare SiO_2–TiO_2 photocatalysts.[8, 39, 41] The direct synthesis of SiO_2–TiO_2 photocatalysts involves the incorporation of TiO_2 and SiO_2 precursors into synthesis solution, followed by the introduction of TiO_2 species into the rod-shaped mesoporous SiO_2 structure. Wu et al.[42] directly synthesized mesoporous TiO_2–SiO_2 composites through a hydrothermal method using $TiCl_3$ solution and tetraethyl orthosilicate (TEOS) as precursors, as well as triblock copolymer P123 ($EO_{20}PO_{70}EO_{20}$) as template, under weak acidic conditions in the presence of zinc acetate. The fabricated TiO_2–SiO_2 composites exhibited high catalytic activity in isopropanol photodegradation, which could be due to the framework of the material and surface titanium species. Witte et al.[43] proposed an in situ synthesis approach to prepare TiO_2/SBA-15. In this method, TiO_2 was added during SBA-15 synthesis to fabricate TiO_2–SiO_2 mesoporous composites with photocatalytic activity and adsorption capacity. Post-synthesis procedure involved TiO_2 deposition on the surface of the pre-prepared mesoporous SiO_2 material through solvent evaporation, impregnation, precipitation, or grafting. Dong et al.[44] obtained mesostructured TiO_2–SiO_2 composites by using titanium isopropoxide and TEOS as precursors and triblock copolymer P123 as template through a co-self-assembly process integrated with solvent evaporation in the presence of large amounts of HCl. Acosta-Silva et al.[45] prepared SBA-15 with different amounts of TiO_2 (TiO_2/SBA-15) through post-synthesis of the previously synthesized SBA-15. TiO_2 particles were then loaded on the SBA-15 surface. Fukuda et al.[35] also synthesized Ti-containing porous SiO_2 by grafting titanium(IV) acetylacetonate onto the surfaces of porous SiO_2 supports, namely, mesoporous SiO_2 MCM-41 and SBA-15, as well as nanoporous SiO_2 HUS-6. Nevertheless, these reported methods present several limitations.[41] In direct synthesis, although Ti species are uniformly distributed in the mesoporous framework, the obtained SiO_2–TiO_2 photocatalyst normally possesses low surface area and TiO_2 loading affects the formation of the mesoporous structure. In post-synthesis, the loading amount of TiO_2 is difficult to control and TiO_2 displays poor dispersibility on the SBA-15 surface in the as-obtained SiO_2–TiO_2 photocatalyst. Therefore, a new synthesis strategy must be developed to address these limitations.

In this work, we report a novel method of surface modification of a mesoporous material through iron(III)-mediated ARGET ATRP on the surfaces of short rod-shaped mesoporous SiO_2 by using $FeCl_3{\cdot}6H_2O$ as catalyst, triphenylphosphine (PPh_3) as ligand, and ascorbic acid (Vc) as reducing agent. For the first time, amphiphilic polymer, namely polyglycidyl methacrylate (PGMA)-polyoligo(ethylene glycol) methyl ether methacrylate (PEGMA), was grafted onto rod-shaped mesoporous SiO_2 through ARGET ATRP. Tetrabutyl titanate (TBT) was hydrolyzed among PEGMA segments through hydrogen bonding because of PEGMA hydrophilicity. Rod-shaped SiO_2@TiO_2 composites were prepared by thermal

removal of PGMA-PEGMA from the prepared SiO_2-PGMA-PEGMA-TiO_2. The novelties of the fabricated short rod-shaped mesoporous SiO_2@TiO_2 hybrid composites compared with previously reported ones mainly include the following aspects. First, SiO_2-PGMA-PEGMA hybrid composites were easily fabricated through ARGET ATRP. The proposed method can be used to modify SiO_2 surfaces by using a wide range of polymers to optimize the attachment of various molecules on the surface. Second, immobilization of TiO_2 nanoparticles through direct embedding in a polymer matrix causes inaccessibility of numerous particles, thereby considerably decreasing photocatalytic efficiency. In the study, amphiphilic copolymer was grafted on mesoporous SiO_2 as template to synthesize rod-shaped mesoporous SiO_2@TiO_2. Removal of the PGMA-PEGMA polymer layer and TiO_2 crystallization were simultaneously conducted during calcination to form a SiO_2@TiO_2 mesoporous structure with a large specific surface area and a high absorption rate, which are vital for increasing catalytic efficiency. Furthermore, the proposed method can avoid the aggregation of TiO_2 nanoparticles, thereby increasing catalytic efficiency.

Results and Discussion

Preparation of short rod-shaped mesoporous SiO_2@TiO_2

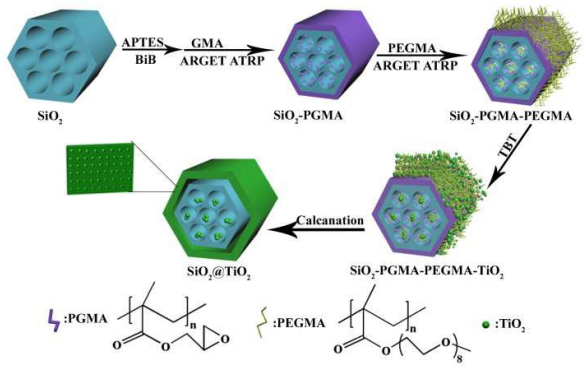

Scheme 1. Schematic of the preparation of short rod-shaped mesoporous SiO_2@TiO_2 on modified mesoporous SiO_2 by ARGET ATRP.

Scheme 1 illustrates the preparation of rod-shaped mesoporous SiO_2 grafted with PGMA-PEGMA amphiphilic diblock copolymer through ARGET ATRP, as well as the synthesis of SiO_2@TiO_2 structure through hydrolysis and condensation of TBT composite materials. The ARGET ATRP system utilized $FeCl_3 \cdot 6H_2O$ as the catalyst in the presence of a limited amount of air. Mesoporous SiO_2, with a diameter of 350–450 nm and a length of 1–1.5 μm, were initially prepared through traditional methods. SiO_2-NH_2 was then prepared by SiO_2 reaction with APTES. The initiator (SiO_2-Br) of ARGET ATRP was obtained through the interaction of SiO_2-NH_2 with BiB. Surface-initiated ARGET ATRP of SiO_2-PGMA-Br was conducted at 60 °C by using SiO_2-Br nanoparticles, with $FeCl_3 \cdot 6H_2O/PPh_3$ as the catalyst and Vc as the reducing agent. SiO_2-PGMA-Br nanoparticles were used as macroinitiators for further polymerization of fresh monomers. Block copolymerization of PEGMA on SiO_2-PGMA surfaces was also conducted using the aforementioned catalyst system. Rod-shaped mesoporous SiO_2 grafted with amphiphilic block copolymer (SiO_2-PGMA-PEGMA) was obtained after polymerization for 15 h at 90 °C. TBT hydrolysis was conducted at 40 °C in a water bath. TBT molecules interacted with the hydrophilic PEGMA units of the amphiphilic copolymer, rather than with the PGMA blocks, through hydrogen bonding. Several small TiO_2 nanoparticles emerged in the parallel channels of mesoporous SiO_2 because of the hydrophilic polymer (PEGMA) grafted inside the mesopores of SiO_2. Rod-shaped mesoporous SiO_2@TiO_2 composite materials were prepared after heating at 450 °C. The composite materials contained TiO_2 shell and bimodal nanoporous structures.

Characterization of rod-shaped SiO_2 polymer

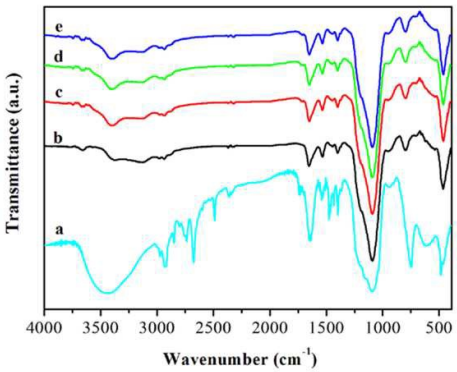

Figure 1. FT-IR spectra of (a) physical mixture of SiO_2-Br and PGMA, (b) SiO_2-PGMA, (c) SiGE1, (d) SiGE2, and (e) SiGE3.

Figure 1 displays the FT-IR spectra of SiO_2-PGMA and SiGE*n*. The peaks at around 3000–2880 cm^{-1} were attributed to the stretching vibrations of CH_3 and CH_2 in PGMA. The peak at 1725 cm^{-1} was assigned to the C=O stretching vibration in PGMA. The peak at 944 cm^{-1} was due to the pendant epoxy group of PGMA in Figure 1b. Moreover, Figure 1a represented the spectra of the physical mixture of SiO_2-Br and PGMA. The absorption peaks at 1725 and 2900 cm^{-1} were characteristic of the C=O group of ester in PGMA and the C–H bending vibrations of methyl groups, respectively. The new absorption bands at 1476 cm^{-1} can be assigned to the twisting vibrations of C–N of SiO_2-Br. Comparison with the FT-IR spectra of SiO_2-PGMA showed that PGMA was successfully grafted onto SiO_2 through ARGET ATRP. After block copolymerization of PEGMA, the absorption peaks at 1725 cm^{-1} were assigned to the C=O group of ester in PGMA and PEGMA. This observation suggested that PEGMA chains were grafted onto SiO_2 through ARGET ATRP. The FT-IR spectra of SiO_2, SiO_2-NH_2, and SiO_2-Br are shown in Figure S1.

Figure 2 shows the FESEM and TEM images of short rod-shaped SiO_2 and SiO_2-PGMA, respectively. Monodispersed rod-shaped SiO_2 particles, with a diameter of 350–450 nm and a length of 1–1.5 μm, are shown in Figures 2a and 2b. The high-

magnification image (inset) in Figure 2a indicates that particles with well-ordered parallel channels are hexagonally facetted. Furthermore, SiO_2-PGMA nanoparticles with a uniform thickness of the polymer layer of approximately 15 nm were obtained after ARGET ATRP. PEGMA grafting resulted in reduced smoothness and clarity of the SiO_2 surface (Figure 3). The uniform polymer layer of SiGE2 was approximately 35 nm (Figure 3c and 3d). In contrast to that of SiGE2, different degrees of aggregation were observed on the surfaces of SiGE1 and SiGE3. The thicknesses of the poorly uniform polymer layers of SiGE1 (Figures 3a and b) and SiGE3 (Figures 3d and e) were approximately 28 and 31 nm, respectively.

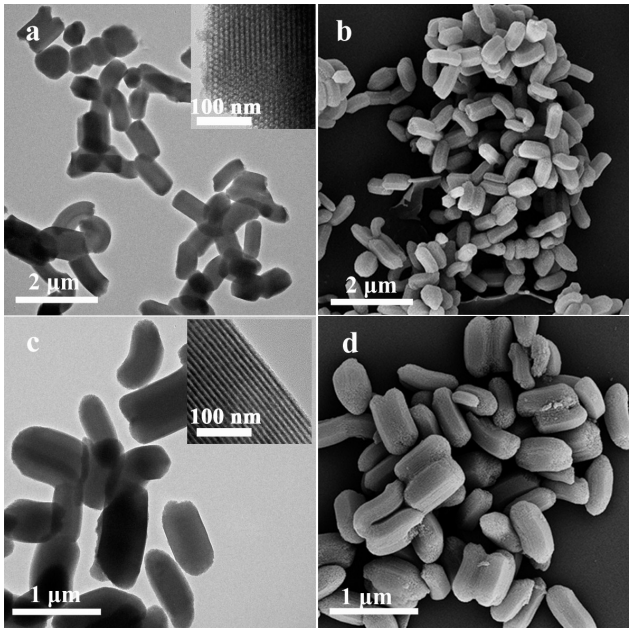

Figure 2. TEM of (a) SiO_2, (c) SiO_2-PGMA and FESEM of (b) SiO_2, (d) SiO_2-PGMA, the insets are the corresponding magnified images of (a) and (c), respectively.

TGA is used to rapidly evaluate the thermal stability and thermal degradation behavior of polymers. The mass retentions of SiO_2-NH_2 and SiO_2-Br at 800 °C were 85.90% and 82.64%, respectively (Figure S2), with organic content losses of 14.10% and 17.36%, respectively. The TGA results of polymer-grated SiO_2 are shown in Figure 4. The weight retention of SiO_2-grafted PGMA nanoparticles at 800 °C was approximately 65.13% (Figure 4a). Using the weight retention of SiO_2-Br nanoparticles (Figure S2c) at 800 °C as the reference, the PGMA weight content relative to that of the SiO_2 core was calculated to be around 21.2%. After PEGMA grafting, the mass retentions of SiGE1, SiGE2, and SiGE3 at 800 °C were 54.08%, 49.65%, and 54.26%, respectively. These results indicated that the larger percentage of weight loss resulted from the decomposition of the grafted PEGMA on the surface of SiO_2 nanoparticles. Thus, PEGMA was successfully grafted onto the SiO_2 surface, and SiGE2 showed a well-controlled polymerization reaction. The mass retention of contrasting samples is shown in Figure S3. Compared with the corresponding samples, the mass retention of the contrast samples was higher, which can be attributed to the weight loss of the surfactants.

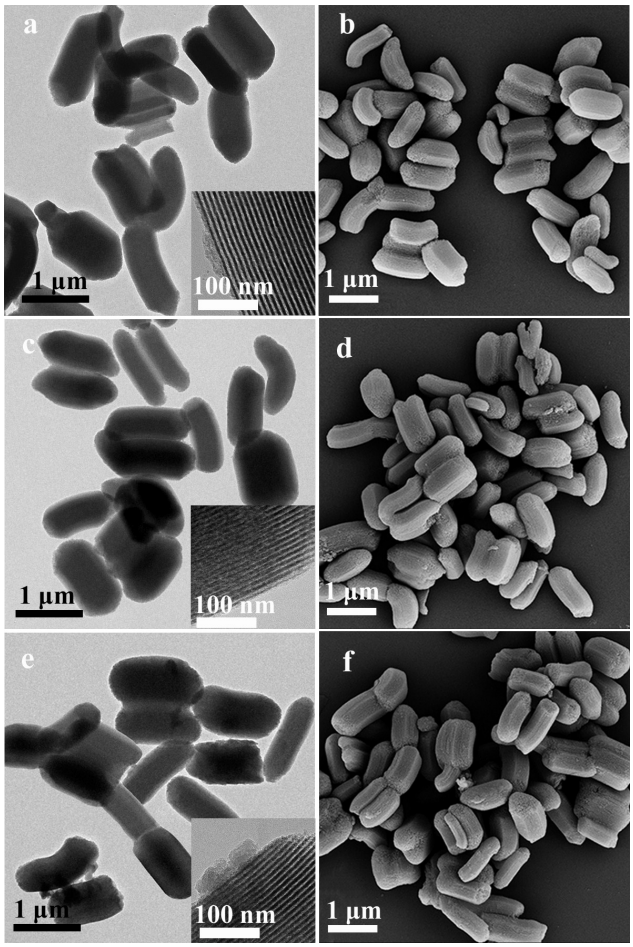

Figure 3. TEM of (a) SiGE1, (c) SiGE2, (e) SiGE3, and FESEM of (b) SiGE1, (d) SiGE2, (f) SiGE3, the insets are the corresponding magnified images of (a), (c) and (e), respectively.

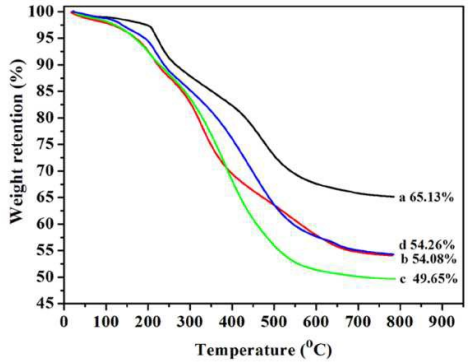

Figure 4. TGA results of (a) SiO_2-PGMA, (b) SiGE1, (c) SiGE2, and (d) SiGE3.

Characterization of short rod-shaped mesoporous SiO_2@TiO_2

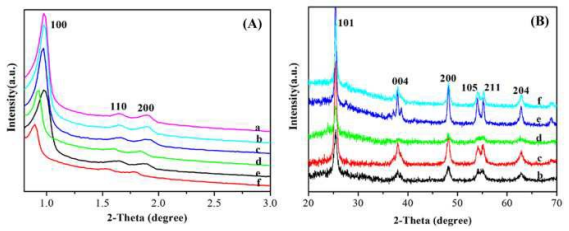

Figure 5. Small-angle (A) and wide-angle (B) XRD patterns of (a) SiO_2, (b) SiO_2@TiO_2-1, (c) SiO_2@TiO_2-2, (d) SiO_2@TiO_2-3, (e) SiO_2@TiO_2-4 and (f) SiO_2@TiO_2-5.

Table 1 Structural properties of short rod-shaped mesoporous SiO_2@TiO_2 samples.

Sample	TiO_2 Crystallite size (nm)	S_{BET} ($m^2\ g^{-1}$)	V ($cm^3\ g^{-1}$)	Pore size (nm)
SiO_2@TiO_2-1	15.4	33.22	0.13	14.4
SiO_2@TiO_2-2	13.9	51.61	0.09	10.1
SiO_2@TiO_2-3	15.8	34.96	0.12	14.9
SiO_2@TiO_2-4	14.8	48.11	0.10	11.4
SiO_2@TiO_2-5	19.4	31.00	0.14	6.1

Typical small-angle XRD patterns of the calcined rod-shaped mesoporous SiO_2 and SiO_2@TiO_2 samples within the range of 0.5°–3° are shown in Figure 5A. All samples exhibited three well-resolved diffraction peaks, which correspond to the (100), (110), and (200) diffraction peaks of the hexagonal features of rod-shaped mesoporous SiO_2; this finding indicated that the samples maintained their ordered pore structure.[36] However, the diffraction intensity of the SiO_2@TiO_2 samples decreased in different degrees, which can be correlated with the slight decrease in the mesoporous order. The diffraction intensity of SiO_2@TiO_2-5 was lower than that of the other samples. The decrease in intensity can be attributed to TiO_2 particles that existed inside the mesopores of the SiO_2 structure, such that the diffraction peaks became weaker because of the loss of diffraction contrast between the wall and the pore.[42] The wide-angle XRD patterns of the calcined SiO_2@TiO_2 in Figure 5B show the characteristic diffraction peaks at 2θ of 25.4°, 37.9°, 48.2°, 53.9°, 55.2°, and 62.9°, which are indexed to the (101), (004), (200), (105), (211), and (204) planes of TiO_2. All the samples were at anatase phases. In addition to the diffraction peaks corresponding to the anatase phase, no other diffraction peaks were observed at 2θ = 20°–70° for all SiO_2@TiO_2 composites; hence, SiO_2 existed in the anatase phase.[46] According to the Scherrer formula, the average crystal sizes of anatase nanocrystallites [calculated from (101) peak] in the calcined samples were within the range of 13.9–19.4 nm. The values are presented in Table 1. The crystallite size of TiO_2 prepared from SiO_2@TiO_2-2 was around 13.9 nm, which is smaller than that (19.3 nm) of TiO_2 prepared from SiO_2@TiO_2-5 without any functional modification. This result could be due to TiO_2 shell collapse during calcination and interparticle aggregation during TBT hydrolysis.

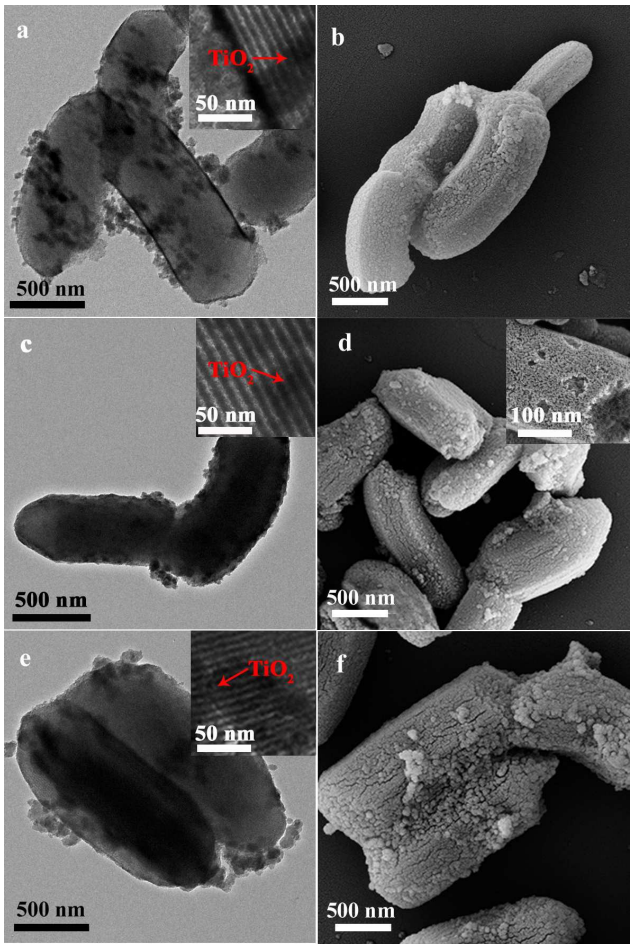

Figure 6. TEM of (a) SiO_2@TiO_2-1, (b) SiO_2@TiO_2-2, (c) SiO_2@TiO_2-3, and FESEM of (a) SiO_2@TiO_2-1, (b) SiO_2@TiO_2-2, (c) SiO_2@TiO_2-3, the insets are the corresponding magnified images of (a), (c), (d) and (e), respectively.

Figure 6 shows the TEM and FESEM images of short rod-shaped mesoporous SiO_2@TiO_2 after calcination at 450 °C. Compared with Figures 2 and 3, Figure 6 shows that the surface morphology of SiO_2@TiO_2 differed from those of SiO_2 and SiO_2-polymer. The TEM images clearly show that the shells of the SiO_2@TiO_2 rods contained small TiO_2 spherical particles, which were formed through aggregation of primary crystallites. SiO_2@TiO_2 was with respect to hollowness and had a rather rough surface because it contained TiO_2 nanoparticles with a diameter of around 14 nm (Figure 6d). This result is consistent with the crystallite size calculated from the XRD data. TEM characterization in the magnified images (inset) in Figure 6d confirmed the presence of TiO_2 deposited on the particle surface. The corresponding magnified images of Figures 6a, 6c,

and 6e clearly display the ordered mesopores in the mesoporous SiO_2 core. Meanwhile, the small TiO_2 nanoparticles emerged in the parallel channels of the mesoporous SiO_2 because of the TBT hydrolysis in the hydrophilic polymer (PEGMA) grafted inside the mesopores of SiO_2. The width of the overall rod was approximately 500 nm, which indicated that TiO_2 nanoparticles formed multilayer precipitation on the surface of rod-shaped SiO_2. The TiO_2 shell of SiO_2@TiO_2-2 was relatively less aggregated compared with those of SiO_2@TiO_2-1 and SiO_2@TiO_2-3. This finding could be attributed to TBT, which interacted with the uniform PEGMA segment molecules of SiGE2 through hydrogen bonding. Furthermore, FESEM results showed that the monodispersity of SiO_2@TiO_2-2 particles (Figure 6d) was also preserved through deposition without interparticle aggregation, in contrast to that of SiO_2@TiO_2-1 (Figure 6b) and SiO_2@TiO_2-3 (Figure 6f). Consequently, the TEM and FESEM images showed that the SiO_2 core was successfully coated with the TiO_2 shell, thereby forming a rough surface morphology. The TEM and FESEM images of SiO_2@TiO_2-4 and SiO_2@TiO_2-5 are shown in Figure S4. Apparently, TiO_2 nanoparticles exhibited different degrees of aggregation. In addition, the HRTEM image of SiO_2@TiO_2-2 after heat treatment at 450 °C is provided in Figure S5. The lattice fringes corresponding to (101) reflection planes of anatase TiO_2 can be clearly observed, which confirms that the sample consists of nanocrystalline TiO_2 particles with an interplanar d-spacing of 0.35 nm (Figure S5). The selected area electron diffraction pattern of the nanocrystalline particles (Figure S5) also revealed the presence of (101), (004), (200), (105), (211), and (204) anatase TiO_2 concentric diffraction rings. Overall, the results confirmed the polycrystalline nature of TiO_2 particles (consistent with the XRD data).

The distribution of TiO_2 throughout the entire surface of rod-shaped mesoporous SiO_2 was confirmed by examining material composition through EDS at random locations on the sample surface. Figures 7 and S6 show that the SiO_2@TiO_2 sample contained oxygen, silicon, and titanium, thereby confirming that TiO_2 was distributed on the surface of the SiO_2@TiO_2 composite. Elemental analysis indicated that the atom percentages of SiO_2@TiO_2-2 were 60.22% for Ti, 37.06% for O, and 2.72% for Si. Compared with those of other SiO_2@TiO_2 samples, the atom percentages or weight percentages of SiO_2@TiO_2-2 were higher and fitted well with the TEM results (Figures 6 and S4). In addition, the EELS mapping images showed that Ti of the rod-shaped mesoporous SiO_2@TiO_2-2 sample was distributed on the surface without apparent particle aggregation (Figure 8a). In Figures 8b–e, blue, kermesinus, and red colors represent O, Si, and Ti, respectively. The elemental map further showed that Ti species were distributed on the outer surface of the TiO_2@SiO_2-2 composite.

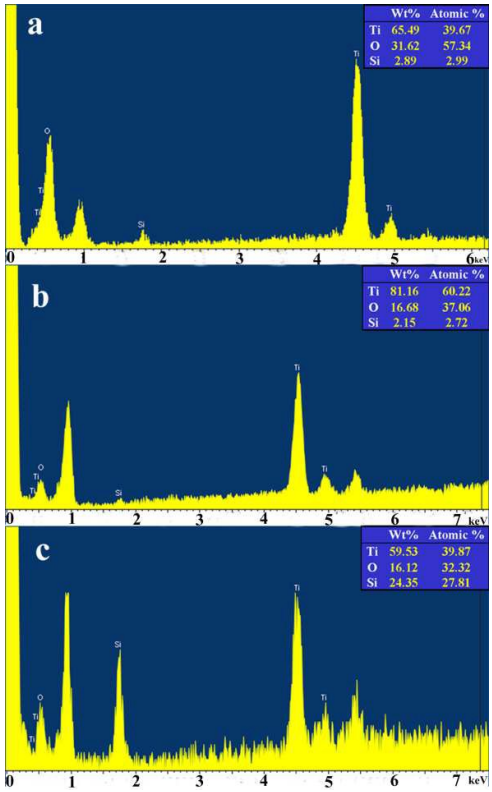

Figure 7. EDS results of (a) SiO_2@TiO_2-1, (b) SiO_2@TiO_2-2, and (c) SiO_2@TiO_2-3.

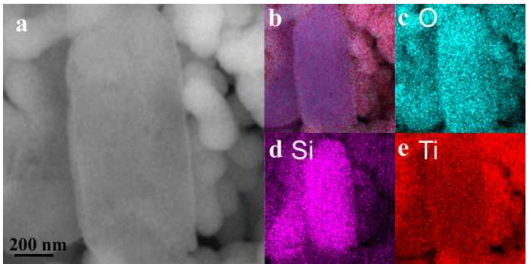

Figure 8. EELS mapping of SiO_2@TiO_2-2.

XPS was conducted to confirm the chemical state of the short rod surface at various stages. Figures 9a–c show the XPS wide scan, C 1s, and O 1s spectra of SiGE2. The survey spectra (Figure 9a) revealed the presence of C, O, and Si. The XPS wide-scan spectrum (Figure 9a) showed two peak components at binding energies (E_b) of about 284 and 532 eV, which are attributed to the C 1s and O 1s species of SiGE2, respectively. Two peaks at E_b of 150.7 and 103.3 eV were also observed in Figure 9a, which can be assigned to Si 2s and Si 2p, respectively. Figure 9b presents the C 1s spectrum of the SiGE2 surface. The thickness of the PGMA-PEGMA polymer layer exceeded the penetration depth of XPS (10 nm). Thus, the chemical composition of the inner surface, where PGMA bonding occurred, was difficult to disclose because the inner surface may be partially exposed to X-ray. Three peak components (Figure 9b) at E_b = 284.6, 286.2, and 288.5 eV are

assigned to C–H/C–C, C–O, and O–C=O species, respectively.[47, 48] Figure 9c shows the high-resolution O 1s scans of SiGE2. In agreement with the literature, the high-resolution O 1s signal can be fitted with three peaks, which correspond to O atoms from the O–C=O (533.4 eV), C–O–C (532.8 eV), and O–C=O (531.9 eV) groups.[49] These results indicated that PGMA-PEGMA prepared through ARGET ATRP was successfully grafted onto the SiO_2 surface. Figures 9d–f show the XPS wide-scan, as well as the Ti 2p and O 1s spectra, of short rod-shaped mesoporous SiO_2@TiO_2-2 after the thermal removal of PGMA-PEGMA (450 °C) from SiGE2-TiO_2. The survey spectrum (Figure 9d) of the SiO_2@TiO_2-2 particles contained only the Ti 2p and O 1s peaks, in addition to C 1s, which is the reference, thereby confirming the complete removal of the polymer. After TBT hydrolysis (Figure 9d), the intensity of C 1s at E_b = 284 eV significantly decreased, with a Ti 2p peak detected at E_b = 460 eV, which is a key indication of the presence of TiO_2 on the SiO_2@TiO_2-2 surface. In the Ti 2p XPS spectrum (Figure 9e), two peaks were observed at 464.2 and 458.5 eV, which belong to Ti $2p_{1/2}$ and Ti $2p_{3/2}$, respectively.[50] This result agreed well with Ti (IV) in pure anatase TiO_2 form. The peak separation of 5.7 eV between the Ti $2p_{1/2}$ and Ti $2p_{3/2}$ signals is also consistent with the reported values in the literature. The high-resolution O 1s spectra of the rod-shaped mesoporous SiO_2@TiO_2-2 sample were determined, as well as their corresponding fitting analysis (Figure 9f). Two single peaks located at around 532.5 and 529.7 eV correspond to the O in Si-O-Si and Ti-O-Ti bonds.[51, 52] The XPS spectra also confirmed the successful functionalization of rod-like SiO_2 through polymer coating followed by deposition with TiO_2 particles.

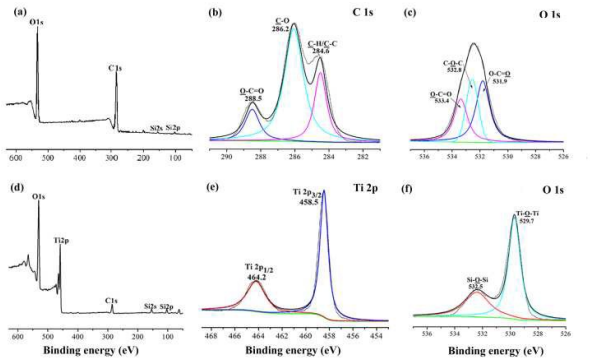

Figure 9. XPS (a) wide scan, (b) C 1s, and (c) O 1s spectra of SiGE2; XPS (d) wide scan, (e) Ti 2p and (f) O 1s spectra of SiO_2@TiO_2-2.

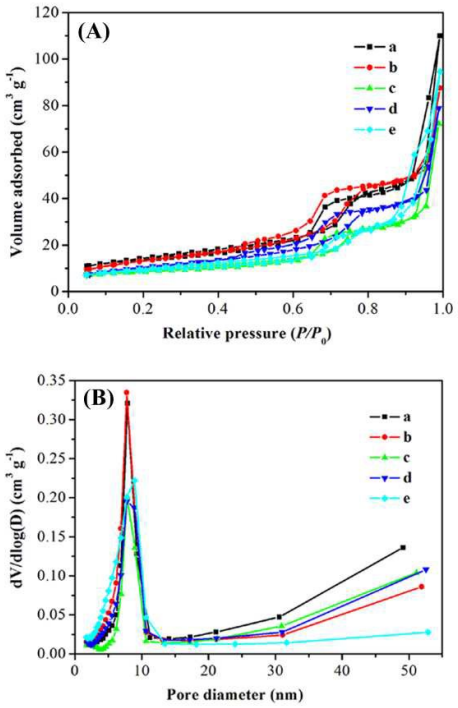

Figure 10. (A) Nitrogen adsorption–desorption isotherms and (B) corresponding pore size distribution curves of (a) SiO_2@TiO_2-1, (b) SiO_2@TiO_2-2, (c) SiO_2@TiO_2-3, (d)SiO_2@TiO_2-4 and (e) SiO_2@TiO_2-5.

Changes in the specific surface area, pore size, and pore volume of short rod-shaped mesoporous SiO_2@TiO_2 were evaluated. The nitrogen adsorption–desorption isotherms of all SiO_2@TiO_2 samples after calcination at 450 °C were established at liquid nitrogen temperature (77 K) and relative pressures (P/P_0) ranging from 0.0 to 1.0. Figure 10 shows the nitrogen adsorption–desorption isotherms and the corresponding pore size distribution plot of the rod-shaped mesoporous SiO_2@TiO_2 composites. According to IUPAC classification, Figure 10A shows types I and IV curves with sharp capillary condensation and evaporation steps in the P/P_0 range of approximately 0.4–0.87 and 0.88–1.0, which indicated very narrow pore size distribution. Within the relative pressure range of 0.4–1.0, the curve of all SiO_2@TiO_2 samples exhibited two small hysteresis loops, with distinct shapes; this finding demonstrated the bimodal pore size distributions in the mesoporous and macroporous regions of inorganic oxides. At a relatively low pressure (between 0.4 and 0.87), the hysteresis loop is classified as type H1,[53] which typically features highly ordered and well-reserved cylinder-type mesopore. However, at a relatively high pressure (between 0.88 and 1.0), the hysteresis loop is categorized as type H3, which is associated with slit-like pores.[54] Figure 10B indicates that rod-like SiO_2@TiO_2 contained bimodal pore size distribution in mesopores and macropores. This type of distribution could be ascribed to two different pores: well-ordered parallel channels or inter-lamellar void and large inter-aggregated pores.[36, 55]

Mesopores resulted from the ordered mesoporous SiO_2 and void yielded by hydrophobic polymer segments between mesoporous SiO_2 and TiO_2 shells after pyrolysis. The removal of the amphiphilic polymer also generated pores. Macropores were formed from large aggregates in the powder. Large pores are associated with large interaggregated pores produced by secondary particles after finer intraaggregated pores formed between intraagglomerated primary particles.[56, 57] This porous structure may provide a convenient transport pathway into the interspace, which is critical for catalysts. Pore structure parameters, such as specific area (S_{BET}), cumulative pore volume (V) and pore diameter, of all the samples are listed in Table 1. Compared with other SiO_2@TiO_2 samples, the SiO_2@TiO_2-2 sample showed relatively larger BET surface area and smaller pore volume, which implied superior adsorption properties. The mesopore size (6.1 nm) of the SiO_2@TiO_2-5 sample was smaller than those of the other SiO_2@TiO_2 samples, with pore sizes ranging from 10.1 nm to 14.9 nm. This finding can be interpreted as follows. Rod-shaped mesoporous SiO_2 without grafted amphiphilic block copolymers possessed relatively large well-ordered parallel channels, which facilitates the emergence of small TiO_2 nanoparticles in the mesopores after TBT hydrolysis. After thermal treatment at 450 °C, TiO_2 nanoparticles were reserved in the mesopores of SiO_2, thereby decreasing pore size.

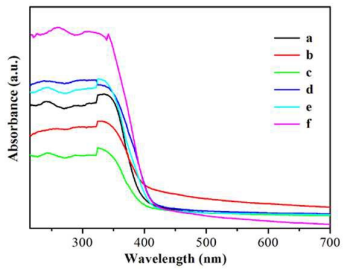

Figure 11. UV-Vis diffuse reflectance spectra of (a) SiO_2@TiO_2-1, (b) SiO_2@TiO_2-2, (c) SiO_2@TiO_2-3, (d) SiO_2@TiO_2-4 (e) SiO_2@TiO_2-5 and (f) pure TiO_2.

To investigate the absorption properties of the rod-shaped mesoporous SiO_2@TiO_2 materials, we measured the UV-Vis diffuse reflectance spectra of all of the SiO_2@TiO_2 samples and pure TiO_2 (Figure 11). Figure 11 demonstrates that a blue shift phenomenon in the SiO_2@TiO_2 composites with respect to that in the pure TiO_2 powder without the mesoporous SiO_2 carrier. This finding implies that the TiO_2 nanoparticles can be dispersed into the mesoporous silica frameworks.[32] TiO_2 is a large-band-gap semiconductor, and the blue shift is attributed to the well-known quantum size effect on semiconductors as the particle size decreases.[45] The blue shift of the adsorption edge indicated the increase in the forbidden band energy. Hence, the blue shift of the absorption edge of the UV–Vis scattering pattern showed the smaller TiO_2 particle size. This result suggests that the modified mesoporous SiO_2 support prevented the aggregation and improved the dispersity of TiO_2 particles.

RhB degradation in aqueous solution under UV light was tested to explore the catalytic activity of different short rod-shaped mesoporous SiO_2@TiO_2 samples. The results are shown in Figure 12. For a better comparison of photocatalytic efficiency among all the samples, the kinetic analysis of RhB degradation was first discussed. The kinetic linear simulation curves (Figure 12A) of the photocatalytic degradation of RhB in all the SiO_2@TiO_2 samples showed that the degradation reaction followed a Langmuir Hinshelwood apparent first-order kinetics model. All these plots match the first-order reaction kinetics well. The apparent reaction rate constant (k) can be calculated from the rate equation $\ln(C_t/C_0) = -kt$. The k values determined for SiO_2@TiO_2-1, SiO_2@TiO_2-2, SiO_2@TiO_2-3, SiO_2@TiO_2-4, SiO_2@TiO_2-5, and P25 were 0.91, 1.41, 0.61, 1.15, 0.55, and 0.85, respectively. The photocatalytic reactivities of the samples showed the following order: SiO_2@TiO_2-2 > SiO_2@TiO_2-4 > SiO_2@TiO_2-1 > P25 > SiO_2@TiO_2-3 > SiO_2@TiO_2-5. The concentration of RhB decreased as UV irradiation time increased (Figure 12B). Approximate 1.3% of RhB molecules were adsorbed on the rod-shaped mesoporous SiO_2@TiO_2 surface when adsorption reached the equilibrium in the dark. The TiO_2 nanoparticles were present in the mesopores of SiO_2 (Figure 6). As UV irradiation time increased, RhB contact with the TiO_2 active species was degraded. The RhB absorbed by mesoporous SiO_2 core then moved to contact with the TiO_2 active species that existed in the mesopores of SiO_2 because of the concentration gradient. Consequently, the RhB absorbed by the mesoporous SiO_2 core became degraded. After UV-vis light irradiation, the concentration of RhB decreased with increasing UV irradiation time. Notably, the mesoporous SiO_2@TiO_2-1, SiO_2@TiO_2-2, and SiO_2@TiO_2-4 exhibited higher photocatalytic activities than P25. In general, photocatalytic activity depends on a material's dispersion of anatase nanocrystals and the adsorption capacity for the reactant.[41, 44] First, the modified rod-shaped SiO_2 prevented the aggregation of TiO_2 nanoparticles. As a result, the dispersion of the anatase nanocrystals was improved. Second, the mesoporous SiO_2 with high surface area efficiently improved the adsorption capacity for the reactant. Figures 12B a–c show that the photocatalytic activities of SiO_2@TiO_2-1 and SiO_2@TiO_2-3 were lower than that of SiO_2@TiO_2-2. This effect was attributed to the different TiO_2 percentages of the samples, as displayed in Figure 7. Hence, the number of SiO_2@TiO_2-2 active sites was higher than those of SiO_2@TiO_2-1 and SiO_2@TiO_2-3 because of the highest amounts of TiO_2 in these samples. Compared with SiO_2@TiO_2-1 and SiO_2@TiO_2-3, SiO_2@TiO_2-2 prepared from SiGE2–TiO_2 contained more TiO_2 nanoparticles. The SiO_2@TiO_2-4 sample was synthesized on the basis of the use of uncalcined rod-shaped SiO_2 in SiO_2@TiO_2-2. The percentage of RhB degradation in the SiO_2@TiO_2-2 sample reached approximately 97% within 3 h, which was higher than that of SiO_2@TiO_2-4. This occurrence was achieved because the large surface area contributes significantly to the photocatalytic activity.[54] The SiO_2@TiO_2-5 sample prepared from unmodified mesoporous SiO_2 presented the lowest photocatalytic activity compared with the other samples. This attribute was ascribed to the interparticle aggregation of the TiO_2 nanoparticles. In

conclusion, the modification of mesoporous SiO_2 improved the photocatalytic activity of the SiO_2@TiO_2 composites. The structural materials effectively improved photocatalytic activity by introducing a considerable number of TiO_2 active and adsorption sites. Time-dependent UV-vis all-band UV scanning spectral changes in RhB degradation catalyzed by SiO_2@TiO_2-2 are shown in Figure 12C. The UV-vis maximum adsorption peak at 553 nm is a characteristic of RhB. The absorbance considerably decreased at 553 nm with increasing irradiation time. No blue-shift to 498 nm was observed in the absorption maximum at any time of illumination, and no additional peaks appeared in the UV-vis spectra in the last course of the experiment using the SiO_2@TiO_2-2 sample. These results illustrated that the dye was completely degraded and not only photobleached.[58]

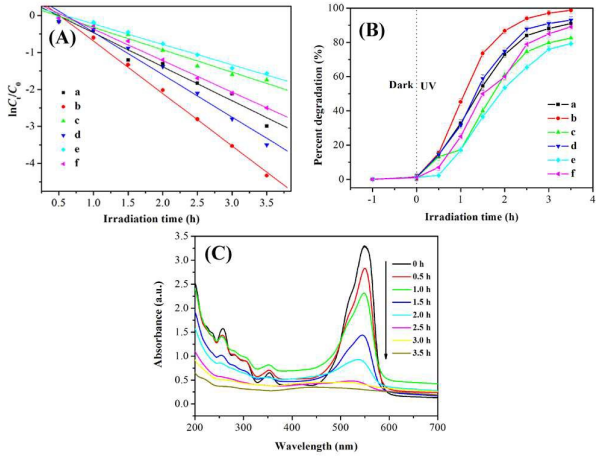

Figure 12. (A) kinetic linear simulation curves of RhB photocatalytic degradation and (B) Percent degradation of RhB as a function of the time of irradiation for (a) SiO_2@TiO_2-1, (b) SiO_2@TiO_2-2, (c) SiO_2@TiO_2-3, (d) SiO_2@TiO_2-4 (e) SiO_2@TiO_2-5 and (f) P25 and (C) UV-Vis spectral profile during the RhB photocatalytic degradation in the presence of SiO_2@TiO_2-2.

Experimental

Materials

Poly(ethylene glycol)-block-poly(propylene glycol)-block-poly(ethylene glycol) (P123, $EO_{20}PO_{70}EO_{20}$), $FeCl_3 \cdot 6H_2O$ (>99%), tetraethoxysilane (TEOS, >99%), TBT (98%), triethylamine (>99.0%), and Vc (>99.7%) were purchased from Sinopharm Chemical Reagent Co. (Shanghai, China). 3-Aminopropyltriethoxysilane (APTES, 99%), ethyl-2-bromoisobutyrate (EBiB, 98%), 2-bromoisobutyryl bromide (BiB; 97%), glycidyl methacrylate (GMA, 97%) and oligo(ethylene glycol)methyl ether methacrylate (EGMA, M_n = 475) were purchased from Sigma-Aldrich (St. Louis, MO, USA). GMA and EGMA were also purified by passing through a column filled with basic alumina and stored at −18 °C before use. PEG (M_W = 6000, Sinopharm Chemical Reagent Co., Ltd., chemical purity), tetrahydrofuran (THF), PPh_3(>99%), N,N-dimethylformamide (DMF), toluene, rhodamine B (RhB) and all other chemicals were obtained from Tianjin Chemical Agent Company (China) and used as received unless otherwise mentioned.

Synthesis and modification of short rod-shaped mesoporous SiO_2

In typical synthesis, PEG and P123 were used as structure-directing agents. At the first stage, HCl, H_2O, P123, and PEG were mixed at a molar ratio of 1:33.63:0.0030:0.0015 and used as starting solution. After vigorous stirring for 3 h at 35 °C, a specific amount of TEOS (molar ratio TEOS: P123: PEG = 1:0.017:0.0088) was added and mixed to the solution under vigorous stirring. The reaction solution was then stirred at 35 °C for 20 h, placed in a Teflon-lined autoclave, heated, and stored at 100 °C for 24 h under static conditions. The white solid products were collected by filtration, washed with water, and air dried at room temperature. The products were then calcined in a tube furnace at 500 °C under flowing air for 4 h to remove the organic template. Amino-functionalized SiO_2 nanoparticles (SiO_2-NH_2) and bromine-immobilized SiO_2 nanoparticles (SiO_2-Br) were synthesized through the reaction of SiO_2 with APTES and BiB with SiO_2-NH_2; the detailed procedure is described in a previous study.[59]

Synthesis of SiO_2-PGMA-PEGMA by ARGET ATRP

A typical polymerization procedure through ARGET ATRP was as follows. Briefly, 0.0045 g of $FeCl_3 \cdot 6H_2O$, 0.0437 g of PPh_3, 5 mL of GMA, 24 μL of EBiB, 15 mL of DMF, 0.10 g of SiO_2-Br, and 0.0290 g of Vc were mixed and added to a dried ampule under stirring to produce a well-dispersed solution. The mixture was ultrasonicated for 5 min and thoroughly bubbled with N_2 for 30 min to eliminate dissolved oxygen. The ampule was flame sealed and then transferred to an oil bath held by a thermostat at 60 °C under continuous stirring to initiate polymerization. The reaction was terminated after 22 h by opening the flask and exposing the catalyst to air. The ampule was then cooled by immersing in ice water. PGMA-grafted SiO_2 (SiO_2-PGMA) separated through centrifugation was exhaustively washed with THF and dried under vacuum to a constant weight at 50 °C.

Surface-initiated block copolymerization of EGMA with a [EGMA]/[$FeCl_3 \cdot 6H_2O$]/[PPh_3]/[Vc]/[EBiB] molar ratio of (890: 940: 990)/1/8/30/3 was conducted on the SiO_2-PGMA surface by using alkyl halogen groups at the chain end of the grafted PGMA as ARGET ATRP macroinitiators. The procedure was similar to that used for surface-initiated ARGET ATRP of GMA. The reaction was terminated upon reaching the desired conversion or after a predetermined time. The SiO_2-PGMA-PEGMA samples were denoted as SiGE*n* (SiGE1, SiGE2, and SiGE3), where *n* represents the different molar ratios of EGMA.

Synthesis of short rod-shaped mesoporous SiO_2@TiO_2 structure

Dried SiGE*n* powder (approximately 0.0080 g) was dispersed in 50 mL of ethanol under sonication. The mixture was added with 0.46 mL of ammonium hydroxide and then transferred to a water-bath tank at 40 °C. After 30 min, the mixture was added dropwise with 0.5 mL of TBT. The entire reaction lasted for 24 h under continuous magnetic stirring. The obtained SiGE*n*-TiO_2 products were washed with ethanol and deionized

water and then dried in vacuum at room temperature overnight. Rod-shaped mesoporous SiO_2@TiO_2 structure was prepared by thermal treatment of SiGE*n*-TiO_2 in an electric furnace at 450 °C for 6 h, during which PGMA-PEGMA was completely oxidized in air into gaseous products. The final samples were designated as SiO_2@TiO_2-1, SiO_2@TiO_2-2, and SiO_2@TiO_2-3.

For comparison, SiO_2@TiO_2-4 and SiO_2@TiO_2-5 samples were also prepared. SiO_2@TiO_2-4 was synthesized using SiO_2-PGMA-PEGMA-4 (SiGE4) under the same condition as that used to prepare SiO_2@TiO_2-2, except that SiO_2 rod was not calcined. SiO_2@TiO_2-5 sample was directly obtained through TBT hydrolysis without any modification on the mesoporous SiO_2 surface.

Photocatalytic activity measurement

The adsorption and photocatalytic activities of the short rod-shaped mesoporous SiO_2@TiO_2 samples were investigated through photodegradation of rhodamine B (RhB) in aqueous solution placed in a quartz glass reactor under visible light. RhB was degraded under UV illumination by using a 375 W mercury lamp with a double-wall jacket, in which water was circulated to prevent the overheating of the reaction mixture. Before illumination, 0.05 g of SiO_2@TiO_2-*n* was added to RhB (100 mL, 30 mg L^{-1}) and stirred for 1 h without visible light irradiation to establish the adsorption/desorption equilibrium between RhB and the catalyst. Photocatalytic degradation was then performed by stirring RhB solutions with the SiO_2@TiO_2 sample under a high-pressure mercury lamp. The suspension was stirred and bubbled with oxygen at a constant flow rate during irradiation. After 30 min, 10 mL of the suspension was withdrawn to determine changes in the absorbance of the RhB solution before and after UV illumination. After centrifugation at 6000 rpm for 10 min, the concentration of RhB dye aqueous solution was analyzed using a UV-vis spectrophotometer at the maximum absorption wavelength of 553 nm with water as the reference. For comparison, the activity of the corresponding P25 was measured under the same conditions. The photocatalytic efficiency could be evaluated using C_t/C_0. A small value of the ratio is indicative of high efficiency, where C_0 and C_t represent the absorbance of the RhB solution before and after irradiation, respectively. The percentage of RhB degradation can be calculated according to the absorbance from the slope of the graph obtained versus time. The measurements were repeated three times for each photocatalyst drawn from one batch of material, and the results were averaged.

Characterization

Fourier transform infrared (FT-IR) spectra were recorded on an IRPrestige-21 spectrometer with a resolution of 4 cm^{-1} and a scan number of 32 by using compressed KBr pellets containing 1wt% of the sample. Field-emission scanning electron microscopy (FESEM) was performed using a SUPRA™55 microscope operated at 5 kV. The powder products were dispersed in ethanol through sonication for 10 min, dropped onto the Si wafer surface, and dried at 60 °C overnight. The specimens were gold coated through ion sputtering before scanning electron microscopy (SEM) observations. High-resolution transmission electron microscopy (HRTEM) was performed using a JEOL model instrument (JEM-2100 F) equipped with an energy-dispersive X-ray spectroscopy (EDS) and electron energy loss spectroscopy (EELS) operated at accelerating voltages of 15 and 200 kV, respectively. All samples were dispersed ultrasonically in ethanol and dropped on copper grids. Thermogravimetric analysis (TGA) was performed on a TGA1500 DSP-SP instrument with a heating rate of 20 °C min^{-1} from room temperature to 800 °C under nitrogen atmosphere. X-ray diffraction (XRD) patterns were recorded on a Bruker D8-ADVANCE (40 kV, 40 mA) powder X-ray diffractometer using Cu Kα (λ = 0.15406 nm) radiation. Data were collected from 0.5°–3° (2θ) and 20°–70° (2θ) with a resolution step size of 0.02° and 0.1°, respectively. Sample composition was determined using X-ray photoelectron spectroscopy (XPS) on a PerkinElmer PHI 5300 spectrometer with a monochromatic Mg Kα X-ray source operated at 12.5 kV and 250 W. Survey spectra were recorded within the range of 0–1000 eV, and C 1s with a binding energy of 284.6 eV was used as reference. Surface area, pore volume, and pore size distribution of the samples were measured using a nitrogen adsorption–desorption apparatus (Micromeritics, TriStar 3020). Specific areas of the samples were calculated by Brunauer–Emmett–Teller (BET) method, and pore diameters were estimated from the desorption branches of the isotherms based on the Barrett–Joyner–Halenda model. UV–vis diffuse reflectance spectra (UV–vis DRS) were recorded on a SHIMADZU UV-2600 spectrophotometer.

Conclusions

This work describes the formation of short rod-shaped mesoporous SiO_2@TiO_2 containing TiO_2 shell. We demonstrated for the first time the successful preparation of rod-shaped mesoporous SiO_2@TiO_2 composites using SiO_2-PGMA-PEGMA as template to avoid the aggregation of TiO_2 nanoparticles. SiO_2-PGMA-PEGMA nanocomposites were prepared through ARGET ATRP on the rod-shaped mesoporous SiO_2 surface. The hydrolyzed TBT molecules interacted with the PEGMA units of the amphiphilic copolymer through hydrogen bonding. Compared with the samples prepared from non-mesoporous or unmodified rod-shaped SiO_2, the rod-shaped mesoporous SiO_2@TiO_2 materials with bimodal nanoporous structures had larger specific surface area and higher absorption rate, which thus enhanced the photocatalytic activity under visible light. The method for preparing short rod-shaped mesoporous SiO_2@TiO_2 can be extended to other shells of mesoporous compositions. This work provides a new pathway for design and fabrication of novel photoactive materials for practical applications in environmental cleaning.

Acknowledgements

This work was supported by the National Natural Science Foundation of China (Grant nos. 51372124, 51572134) and the Programfor Scientific Research Innovation Team in Colleges and Universities of Shandong Province.

Notes and references

1 C. T. Kresge, M. E. Leonowicz, W. J. Roth, J. C. Vartuli and J. S. Beck, *Nature*, 1992, 359, 710.
2 G. W. Zhou, K. K. Fung, L. W. Wong, Y. J. Chen, R. Renneberg and S. H. Yang, *Talanta*, 2011, 84, 659.
3 F. Q. Yu, X. D. Tang and M. S. Pei, *Microporous Mesoporous Mater.*, 2013, 173, 64.
4 L. Yuan, Q. Q. Tang, D. Yang, J. Z. Zhang, F. Y. Zhang and J. H. Hu, *J. Phys. Chem. C*, 2011, 115, 9926.
5 D. W. Lee, M. H. Jin, C. B. Lee, D. Oh, S. K. Ryi, J. S. Park, J. S. Bae, Y. J. Lee, S. J. Park and Y. C. Choi, *Nanoscale*, 2014, 6, 3483.
6 M. A. Smith, M. G. Ilasi and A. Zoelle, *J. Phys. Chem. C*, 2013, 117, 17493.
7 L. Cao, T. Man and M. Kruk, *Chem. Mater.*, 2009, 21, 1144.
8 J. Y. Kim, J. Y. Kim, H. J. Kang, W. Y. Kim, Y. H. Lee and J. S. Lee, *Inorg. Chem.*, 2014, 53, 5884.
9 J. Luo, J. Y. Yu, R. J. Gorte, E. Mahmoud, D. G. Vlachos and M. A. Smith, *Catal. Sci. Technol.*, 2014, 4, 3074.
10 P. Pasetto, H. Blas, F. Audouin, C. Boissière, C. Sanchez, M. Save and B. Charleux, *Macromolecules*, 2009, 42, 5983.
11 X. Li, C. Y. Hong and C. Y. Pan, *Polymer*, 2010, 51, 92.
12 S. Bhattacharyya, H. Wang and P. Ducheyne, *Acta Biomater.*, 2012, 8, 3429.
13 J. Moreno and D. C. Sherrington, *Chem. Mater.*, 2008, 20, 4468.
14 Y. Z. Zhang, Y. Wang and K. Matyjaszewski, *Macromolecules*, 2011, 44, 683.
15 S. Banerjee, T. K. Paira and T. K. Mandal, *Polym. Chem.*, 2014, 5, 4153.
16 M. Wang, J. Yuan, X. B. Huang, X. M. Cai, L. Li and J. Shen, *Colloids Surf. B Biointerfaces*, 2013, 103, 52.
17 B. T. Cheesman, J. D. Willott, G. B. Webber, S. Edmondson and E. J. Wanless, *ACS Macro Lett.*, 2012, 1, 1161.
18 L. Cao and M. Kruk, *Polym. Chem.*, 2010, 1, 97.
19 L. Cao, T. Man, J. Q. Zhuang and M. Kruk, *J. Mater. Chem.*, 2012, 22, 6939.
20 M. Kruk, *Isr. J. Chem.*, 2012, 52, 246.
21 M. Kruk, B. Dufour, E. B. Celer, T. Kowalewski, M. Jaroniec and K. Matyjaszewski, *Macromolecules*, 2008, 41, 8584.
22 C. Y. Zha, L. M. Shen, X. Y. Zhang, Y. F. Wang, B. A. Korgel, A. Gupta and N. Z. Bao, *ACS Appl. Mater. Interfaces*, 2014, 6, 122.
23 X. X. Wang, M. Xi, H. Fong and Z. T. Zhu, *ACS Appl. Mater. Interfaces*, 2014, 6, 15925.
24 J. Yun, S. H. Hwang and J. Jang, *ACS Appl. Mater. Interfaces*, 2015, 7, 2055.
25 F. E. Osterloh, *Chem. Mater.* 2008, 20, 35.
26 J. M. Wu, *J. Phys. Chem. C*, 2008, 112, 13192.
27 S. Lee, J. Lee, S. H. Hwang, J. Yun and J. Jang, *ACS nano*, 2015, 9, 4939.
28 F. J. Chen, G. W. Zhou, H. J. Chen, B. Sun and Y. Zhang, *RSC Adv.*, 2014, 4, 41678.
29 H. Jeon, C. S. Lee, R. Patel and J. H. Kim, *ACS Appl. Mater. Interfaces*, 2015, 7, 7767.
30 M. G. Wang, J. Han, H. X. Xiong, R. Guo and Y. D. Yin, *ACS Appl. Mater. Interfaces*, 2015, 7, 6909.
31 J. Ma, J. Chu, L. S. Qiang and J. Q. Xue, *RSC Adv.*, 2012, 2, 3753.
32 X. F. Qian, T. Kamegawa, K. Mori, H. X. Li and H. Yamashita. *J. Phys. Chem. C*, 2013, 117, 19544.
33 Z. J. Ma, W. B. Chen, Z. L. Hu, X. Z. Pan, M. Y. Peng, G. P. Dong, S. F. Zhou, Q. Y. Zhang, Z. M. Yang and J. R. Qiu, *ACS Appl. Mater. Interfaces*, 2013, 5, 7527.
34 W. T. Qiao, G. W. Zhou, X. T. Zhang and T. D. Li, *Mater. Sci. Eng. C*, 2009, 29, 1498.
35 M. Fukuda, N. Tsunoji, Y. Yagenji, Y. Ide, S. Hayakawa, M. Sadakane and T. Sano, *J. Mater. Chem. A*, 2015, 3, 15280.
36 M. N. Zhao, G. W. Zhou, L. Zhang, X. Y. Li, T. D. Li and F. F. Liu, *Soft Matter*, 2014, 10, 1110.
37 Y. Yu, M. Z. Zhang, J. Chen and Y. D. Zhao, *Dalton Trans.*, 2013, 42, 885.
38 X. Y. Li and J. H. He, *ACS Appl. Mater. Interfaces*, 2013, 5, 5282.
39 F. Bérubé, B. Nohair, F. Kleitz and S. Kaliaguine, *Chem. Mater.*, 2010, 22, 1988.
40 R. Jorge, G. A. Aída, S. M. Felipe, M. A.Víctor, C. V. Perla, O. Laetitia and M. Françoise, *Energy Fuels*, 2012, 26, 773.
41 S. C. Zhang, D. Jiang, T. Tang, J. H. Li, Y. Xu, W. L. Shen, J. Xu and F. Deng, *Catal. Today*, 2010, 158, 329.
42 Z. Y. Wu, Y. F. Tao, Z. Lin, L. Liu, X. X. Fan and Y. Wang, *J. Phys. Chem. C*, 2009, 113, 20335.
43 K. D. Witte, A. M. Busuioc, V. Meynen, M. Mertens, N. Bilba, G. V. Tendeloo, P. Cool and E. F. Vansant, *Microporous Mesoporous Mater.*, 2008, 110, 100.
44 W. Y. Dong, Y. J Sun, C. W. Lee, W. M. Hua, X. C. Lu, Y. F. Shi, S. C Zhang, J. M. Chen and D. Y. Zhao, *J. Am. Chem. Soc.*, 2007, 129, 13894.
45 Y. J. Acosta-Silva, R. Nava, V. Hernández-Morales, S. A. Macías-Sánchez, M. L. Gómez-Herrera and B. Pawelec, *Appl. Catal. B*, 2011, 110, 108.
46 M. Kruk, B. Dufour, E. B. Celer, T. Kowalewski, M. Jaroniec and K. Matyjaszewski, *J. Phys. Chem. B*, 2005, 109, 9216.
47 C. Y. Li, F. J. Xu and W. T. Yang, *Langmuir*, 2013, 29, 1541.
48 C Huang, K. G. Neoh and E. T. Kang, *Langmuir*, 2012, 28, 563.
49 R. Barbey, V. Laporte, S. Alnabulsi and H. A. Klok, *Macromolecules*, 2013, 46, 6151.
50 C. Liu, D. Yang, Y. Jiao, Y. Tian, Y, G. Wang and Z. Y. Jiang, *ACS Appl. Mater. Interfaces*, 2013, 5, 3824.
51 D. P. Wang and H. C. Zeng, *Chem. Mater.*, 2009, 21, 4811.
52 G. Lassaletta, A. Fernández, J. P. Espinós and A. R. González-Elipe, *J. Phys. Chem.*, 1995, 99, 1484.
53 G. Q. Zu, J. Shen, W. Q. Wang, L. P. Zou, Y. Lian and Z. H. Zhang, *ACS Appl. Mater. Interfaces*, 2015, 7, 5400.
54 X. C. Li, V. T. John, J. J. Zhan, G. H. He, J. B. He and L. Spinu, *Langmuir*, 2011, 27, 6252.
55 C. F. Wang, G. W. Zhou, Y. Q. Xu and J. Chen, *J. Phys. Chem. C*, 2011, 115, 22191.
56 G. K. Zhang, X. M. Ding, F. S. He, X. Y. Yu, J. Zhou, Y. J. Hu and J. W. Xie, *Langmuir*, 2008, 24, 1026.
57 J. Liu Y. J. Hu, F. Gu and C. Z. Li, *Ind. Eng. Chem. Res.*, 2009, 48, 735.
58 P. Wilhelm and D. Stephan, *J. Photochem. Photobiol. A Chem.*, 2007, 185, 19.
59 J. T. Sun, C. Y. Hong, and C. Y. Pan, *J. Phys. Chem. C*, 2010, 114, 12481.

Fabrication and Photoactivity of Short Rod-shaped Mesoporous SiO_2@TiO_2 Composites with TiO_2 Shell

Pei Cao, Guowei Zhou,* Yixian Ren, and Hong Xiao

Key Laboratory of Fine Chemicals in Universities of Shandong, School of Chemistry and Pharmaceutical Engineering, Qilu University of Technology, Jinan 250353, Shandong, People's Republic of China

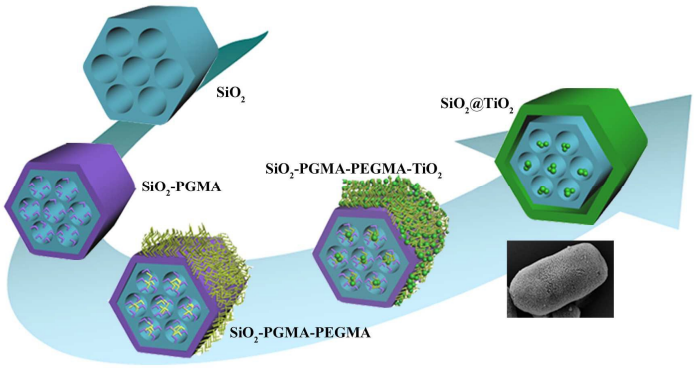

Short rod-shaped mesoporous SiO_2@TiO_2 composites containing TiO_2 shell were prepared using short rod-shaped mesoporous SiO_2-PGMA- PEGMA as template and TBT as titanium source.